RESEARCH ARTICLE

National Science Review
: output,
doi: https://doi.org/

NEUROSCIENCE

Lifespan Development of EEG Alpha and Aperiodic Component Sources is Shaped by the Connectome and Axonal Delays

Ronaldo Garcia Reyes[1,2,3*,†], Ariosky Areces Gonzalez[1,3,4], Ying Wang[1,3], Yu Jin[1,3], Shahwar Yasir [1,3], Maria Luisa Bringas-Vega [1,3], Mitchell Valdes-Sosa [2,3], Cheng Luo [1,3], Peng Xu [5], Viktor Jirsa [6], Dezhong Yao [1,3], Ludovico Minati[1,3,7] and Pedro A. Valdes–Sosa[1,2,3*,†]

[1] Clinical Hospital of Chengdu Brain Science Institute, University of Electronic Science and Technology of China, Chengdu 610054, China; [2] Neuroinformatics, Cuban Neurosciences Center, 11300, Havana, Cuba; [3] China-Cuba Belt and Road Joint Laboratory on Neurotechnology and Brain-Apparatus Communication, University of Electronic Science and Technology of China, Chengdu, P. R. China; [4] School of Technical Sciences, University "Hermanos Saiz Montes de Oca" of Pinar del Río, Pinar del Río, Cuba; [5] Laboratory for Brain Science and Artificial Intelligence, Southwest University of Science and Technology, Mianyang 621010, China; [6] Aix Marseille Université, Institut National de la Santé et de la Recherche Médicale, Institut de Neurosciences des Systèmes (INS) UMR1106; Marseille 13005, France; [7] Center for Mind/Brain Science (CIMeC), University of Trento, 38123, Trento, Italy

ABSTRACT

We introduce ξ–αNET, a model of cortical activity that represents the EEG aperiodic (ξ) and α-rhythm (α) components as Hida–Matérn processes constrained by anatomical connectivity and interareal conduction delays. This approach integrates the decomposition of Spectral Granger Causality and quantifies the lifespan trajectories of spectral processes. Using Bayesian inversion on cross-spectral rsEEG data from 1,965 participants aged 5–100 years (HarMNqEEG dataset), the model estimates cortical activity showing high test-retest reliability, effective connectivity patterns, and conduction delays. Given the approximate cortical hierarchy inferred from the inverted T1w/T2w myelination map, used as a proxy for feedforward and feedback organization, the aperiodic and α components reveal opposite directional networks across the lifespan, where the aperiodic component is localized in the frontal cortex and the α component is localized in the posterior cortex, with feedforward and feedback directed connections, respectively. For both processes, we found that the spectral parameters follow a nonlinear inverted U-shape lifespan trajectory. Finally, the model uniquely estimates global conduction delays, which were negatively correlated with α frequency and with independent cortical myelination (T1w/T2w) measures, consistent with a mechanistic link between conduction delays and α-rhythm modulation.

Keywords: Lifespan, Spectral Components, EEG-Dataset, Conduction Delays, Source Analysis, Alpha-Rhythms

INTRODUCTION

Spectral Components Models (SCM) have become a standard framework for decomposing neural oscillations into meaningful constituents. In Table 1, we show a systematic review of the main SCM in the literature. In this paper, we analyze neural oscillations using the cross-spectrum, defined from an EEG vector time series $\mathbf{v}_t \in \mathbb{R}^{N_c \times 1}$:

$$\boldsymbol{\Sigma}_\omega = \mathbb{E}\left[\mathbf{v}_\omega \mathbf{v}_\omega^\dagger\right] \in \mathbb{R}^{N_c \times N_c}, \qquad (1)$$

where N_c is the number of sensors, $\mathbb{E}$ its the expectation over time trials, $\mathbf{v}_\omega$ represents the Fourier transform of the EEG signal, the symbol $(\cdot)^\dagger$ denotes conjugate transpose., and $\boldsymbol{\Sigma}_\omega$ denotes the cross-spectrum at frequency ω. The diagonal elements $\boldsymbol{\Sigma}_{\omega,ii}$ capture power spectra of individual channels, while the off-diagonal elements reveal channel interactions.

Across the literature, two key Spectral Components (SC) consistently emerge (Fig. 1): the Aperiodic Component (ξ-process), characterized by a monotonic decay with frequency, and the Periodic Component with a notable resonant peak in the α-band, 7–13 Hz), known as the α-process [2,6,11,12]. The ξ-process is sometimes approximated by a $1/\omega^\beta$ decay, representing a fractional Brownian process in the time domain.

Two complementary approaches have historically shaped SCM development (Table 1). The foundational work of Zetterberg *et al.* [1] employed a time-domain approach using Autore-

---

*Corresponding authors. Email: gaussn0ise29@gmail.com, pedro.valdes@neuroinformatics-collaboratory.org. †Equally contributed to this work..

Received: XX XX Year;
Revised: XX XX Year;
Accepted: XX XX Year

Table 1. Comparison of the main Spectral Components Models (SCM). All SCM approximate the Aperiodic Component as a Matérn process or its limiting cases.

Model	Components Distribution			Scale	Cross	Non-Stationary	Anat-Priors	ESI	Connectivity	Ref.
	AC	α-Peak	Others							
Zetterberg	AR(1)	AR(2)	—	1	—	—	—	—	—	[1]
ξ-α	$\mathcal{M}$	$\mathcal{HM}$	—	1	—	—	—	—	—	—
Multi ξ-α	$\mathcal{M}$	$\mathcal{HM}$	—	1	✓	—	—	—	—	[2]
Dipolar ξ-α	$\mathcal{M}$	$\mathcal{HM}$	—	1	✓	—	—	Dipolar	Functional	[3]
BOSC	$\mathcal{M}$	χ^2	χ^2	log-log	—	—	—	—	—	[4]
IRASA	$\mathcal{M}$	—	—	log-log	—	✓	—	—	—	[5]
FOOOF	$\mathcal{M}$	$\mathcal{N}$	$\mathcal{N}$	log	—	✓	—	MNE	—	[6]
SPRiNT	$\mathcal{M}$	$\mathcal{N}$	$\mathcal{N}$	log	—	✓	—	—	—	[7]
PAPTO	$\mathcal{M}$	$\mathcal{N}$	$\mathcal{N}$	log	—	✓	—	—	—	[8]
ξ–π	Monotonic	Unimodal	Unimodal	1	—	—	—	—	—	[9]
Cortical ξ-α	$\mathcal{M}$	$\mathcal{HM}$	—	1	✓	—	—	eLORETA	Functional	[10]
ξ-αNET	MVAR + $\mathcal{M}$	MVAR + $\mathcal{HM}$	—	1	✓	—	✓	Bayesian	Effective	—

Note: Dist: statistical distribution assumed for each component — AR: Autoregressive model; $\mathcal{M}$: Matérn process; $\mathcal{HM}$: Hida–Matérn process; $\mathcal{N}$: Gaussian (normal); χ^2: chi-squared; Monotonic: constrained monotonic shape; Unimodal: single-peak shape. Scale: frequency axis scaling — 1: linear; log: logarithmic; log-log: log-power vs. log-frequency. Cross: multivariate modeling of the cross-spectra. Non-Stat: non-stationary modeling capability. Anat-Priors: use of structural priors like Connectome + Delays. ESI: type of electrophysiological source imaging used (e.g., MNE, eLORETA, Bayesian). Connectivity: Functional: undirected association; Effective: directed/causal influence models.

gressive Moving Average (ARMA) models to estimate EEG spectra. In contrast, Pascual-Marqui *et al.* [2] pioneered a frequency domain approach with the ξ-α model, representing EEG spectra as a mixture of independent stochastic processes: the ξ and α-processes. Pascual's adoption of a generalized Lorentzian profile—originally inspired by spectroscopy—enabled efficient fitting to EEG spectra (note Fig. 1). Subsequent work by Amador *et al.* [13] shows the success of this model in capturing developmental changes. As we show, the Lorentzian spectral profiles that characterize the ξ-α model arise from time-domain processes governed by the Hida–Matérn class. This connection extends beyond the aperiodic component, suggesting that all EEG components are driven by fractional stochastic dynamics, a viewpoint missing in contemporary SCM.

Recent SCM have diversified, adopting the frequency-domain framework introduced by Pascual through the ξ–α model (Table 1). Univariate SCM such as BOSC [4], IRASA [5], FOOOF [6], SPRiNT [7], PAPTO [8], and the recent ξ–π model [9] offer a range of parametric and non-parametric teqniques. On the other hand, we also have a multivariate approach to model the off-diagonal elements of the cross-spectra. An early example is the multivariate ξ-α model [2], although it is restricted to sensor-level EEG. Valdés-Sosa *et al.* [3] later proposed the first source-level formulation, modeling ξ as an isotropic process on the cortical surface and α-rhythms as two correlated stochastic dipole processes with fixed orientations and magnitudes. Jirsa *et al.* [14] demonstrated that spatially extended neural fields with homogeneous connectivity and embedded heterogeneous connections can similarly explain ξ–α processes. The rationale in both cases is the same: isotropically distributed sources are causally linked to ξ, and more localized sources are linked to α. More recently, Pascual *et al.* [10] introduce Cortical ξ–α, which extends the ξ–α model to cortical source space using eLORETA for spectral functional connectivity estimation.

As we conclude from (Table 1), current approaches to estimating the neural sources of SC typically follow a two-step strategy: (i) localizing activity to putative source sensors, followed by (ii) fitting SCM parameters. All these methods neglect key anatomical and functional constraints, such as structural connectivity and conduction delays, that shape the spatiotemporal propagation of oscillatory activity [15,16]. As we have previously shown, such a two-step strategy can lead to biased estimates due to misspecified source covariance matrices [17].

Solutions to all these challenges can be found

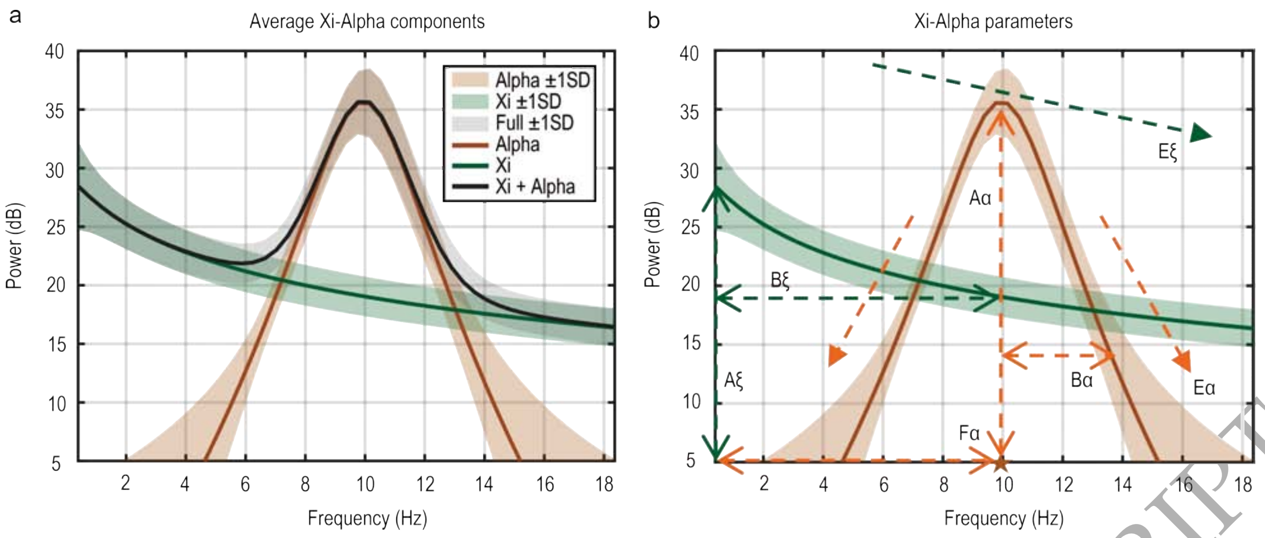

Figure 1. Xi–Alpha spectral decomposition for a representative subject. (a) The empirical EEG power spectrum (gray band) is modeled as a linear superposition of two physiologically interpretable and independent components with generalized Lorentz spectral profiles. The first component, the aperiodic process ξ (green line), captures the characteristic $1/\omega$ spectral decay. The second component, the α-process (orange line), models narrowband oscillatory activity centered within the 7–13 Hz range, corresponding to α-rhythms. The combined ξ–α model (black line) accurately captures the empirical spectral shape by summing the independent contributions of both components. Shaded regions indicate ±1 standard deviation across all EEG sensors of one subject. (b) The components are modeled at each sensor i using a generalized Lorentz spectral distribution given by $\psi(\omega \mid A, B, E, F) = A/(1 + B(\omega - F)^2)^E$, where A is the amplitude (in dB), B is the bandwidth (in s^2), E is the spectral exponent, and F is the frequency shift (in Hz). The aperiodic component is defined as $\xi_{\omega,i} = \psi(\omega \mid A\xi_i, B\xi_i, E\xi_i, 0)$, and the α spectral peak as $\alpha_{\omega,i} = (\psi(\omega \mid A\alpha_i, B\alpha_i, E\alpha_i, F\alpha_i) + \psi(\omega \mid A\alpha_i, B\alpha_i, E\alpha_i, -F\alpha_i))/2$. Here, $A\xi_i$ and $A\alpha_i$ quantify the amplitude of each component; $B\xi_i$ and $B\alpha_i$ control spectral bandwidth; $E\xi_i$ and $E\alpha_i$ determine spectral decay; and $F\alpha_i$, shown by the orange star on the frequency axis, denotes the peak alpha frequency (PAF) and characterizes the modal frequency of the α-rhythms [13].

within large-scale initiatives such as the Digital Twin Brain and The Virtual Brain Project [18, 19], which integrate rich neuroanatomical data to capture neural oscillations more realistically. However, they require substantial computational resources, which limits their direct practical applicability in large-scale normative studies. To overcome these limitations, here we introduce ξ-αNET, a mesoscale generative model of cortical activity formulated as a sparse, structurally constrained network of Hida–Matérn processes. Unlike previous SCM approaches, ξ-αNET allows the joint inference of source-level spectral dynamics and effective connectivity across the lifespan.

RESULTS

Xi-AlphaNET as a Sparse Structurally Constrained Network of Hida-Matérn Process

Forward Model

We propose ξ–αNET, a mesoscale generative model of cortical dynamics that accounts for EEG observations by integrating vertex-wise spectral processes with anatomically grounded structural connectivity and conduction delays. To start, the observed EEG time series $\mathbf{v}_t \in \mathbb{R}^{N_c \times 1}$ is modeled as a linear projection of distributed cortical activity:

$$\mathbf{v}_t = \mathbf{K}\mathbf{j}_t + \mathbf{n}_t, \tag{2}$$

where $\mathbf{K} \in \mathbb{R}^{N_c \times N_v}$ is the lead-field matrix and $\mathbf{n}_t$ is zero-mean gaussian noise. We aim to model the time-domain cortical activity $\mathbf{j}_t \in \mathbb{R}^{N_v}$ at each thalamocortical unit under three constraints: (i) the model must incorporate structural priors, reflecting structural connectivity and conduction delays across neurotracts, that shape the spatiotemporal correlations in a causal way; (ii) the spectral dynamics must arise as a linear superposition of two statistically independent components, corresponding to aperiodic and oscillatory generators; (iii) and the resulting power spectrum must exhibit Lorentzian profiles, consistent with empirical spectra observed across multiple frequency bands in EEG/MEG recordings.

To satisfy the first condition (i), we model the cortical dynamics within a structurally constrained Multivariate Autoregressive (MVAR) network, where the autoregressive coefficients are informed by structural priors. However, simple MVAR or AR models fail to reproduce the full characteristics of Lorentzian spectral profiles of neural oscillations, particularly in the α-band. Therefore, it is necessary to use MVAR with colored innovations.

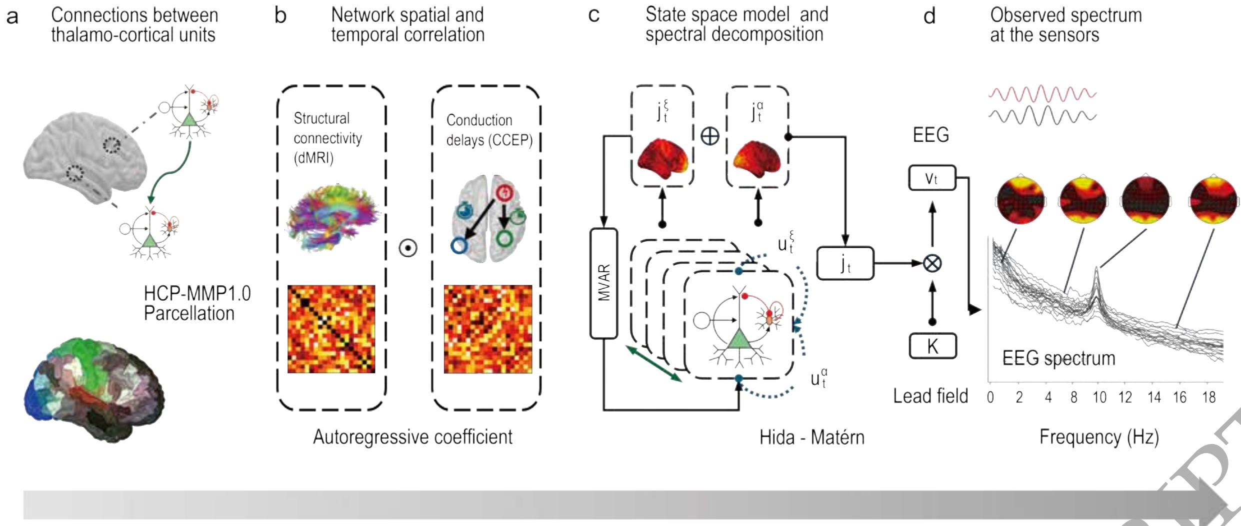

Figure 2. ξ-αNET Forward Model. (a) Connectivity between cortical generators is constrained with structural connectivity from diffusion MRI (dMRI) tractography and conduction delays derived from cortico-cortical evoked potentials (CCEP), where HCP-MMP1 parcellation [20] is used to define the cortical generators. (b) Structural connectivity and conduction delay estimates shape the baseline spatiotemporal correlations of the cortical network. (c) The cortical activity ($\mathbf{j}_t$) arises from the linear superposition of two independent spectral processes, where $\mathbf{j}_t^\xi$ accounts for the aperiodic component and $\mathbf{j}_t^\alpha$ for the α spectral peak. Each activation is modeled using an independent MVAR state-space model with colored Hida-Matern innovations $\mathbf{u}_t^\xi$ and $\mathbf{u}_t^\alpha$. The autoregressive coefficient of the MVAR model is shaped by the connectome and the conduction delays and allows for modeling non-local interactions between cortical generators, while the independent Hida Matern innovations represent local processes at each thalamocortical unit, which allows for introducing Lorenzian spectral profiles for each spectral process, whose parameters have a sparse distribution on the cortical surface. (d) Cortical activity is then projected to the sensor using the lead-field matrix (**K**), yielding observed EEG spectra consistent with electrophysiological data. This framework enables the estimation of cortical SC, conduction delays, and source effective connectivity from EEG/MEG recordings, supporting large-scale normative studies of cortical maturation. The symbol ⊙ denotes the Hadamard (element-wise) product used to introduce a spatiotemporal decomposition of the interactions between generators of neural activity, ⊕ denotes the sum, and ⊗ denotes the standard matrix product.

The second condition (ii) can be warranted if we assume that the cortical activity $\mathbf{j}_t$ is the linear superposition of two independent stochastic processes that model the activations of the independent SC. This approach is aligned with the linear decomposition of the cross-spectrum in SC used on the Multivariate ξ–α proposed by Pascual *et al.* [2,3]. However, despite the success of ξ–α models, the underlying time-domain mechanisms capable of generating Lorentzian spectral profiles have never been explained. Here, we report a formulation that addresses this gap: *Lorentzian spectral profiles can be generated by real-valued fractional stochastic processes belonging to the Matérn class.* These are Gaussian processes with a temporal delayed structure or autocorrelation. Matérn processes have found extensive use in spatial statistics and machine learning. However, the application of this process to model cortical time series has been overlooked within the neuroscience community. As shown in (Table 1), we found that the aperiodic component of neural oscillation can be explained in terms Matérn process, which provides a principled time-domain origin of the ξ-process defined by Pascual *et al.* [2,3].

Resonant spectral peaks, such as those observed in the α process or others, present a significant challenge because they reflect intrinsic oscillatory dynamics that conventional Matérn processes, on their own, cannot fully capture. Early work, such as the thalamocortical Robinson model [21,22], demonstrates that damped differential equations can generate oscillatory modes through the interplay of damping and delays. However, the Robinson model cannot reproduce the full range of spectral patterns observed in the α-band, particularly the Lorentzian spectral profiles with arbitrary exponents, which govern the smoothness of the corresponding time-domain processes introduced by Pascual *et al.* [2,3,10]. Properly modeling these features requires the use of fractional stochastic differential equations, as implemented in oscillatory Matérn processes [23].

Although oscillatory Matérn processes introduce a resonant spectral peak, the time domain representation requires complex-valued stochastic processes [23]. This is inconsistent with the real-valued nature of neurophysiological signals. Therefore, in order to address this limitation, we model the α-rhythm within each thalamocortical unit using the Hida-Matérn process. Unlike the oscillatory Matérn process, the Hida-Matérn formulation yields an analytically tractable, physically interpretable, and real-valued process in a time-domain model that aligns with the expected empirical properties of cortical activity [24]. Importantly, Hida-Matérn processes are exact solutions to fractional stochastic differential equations. This mathematical framework has been successfully applied to complex phenomena such as turbulence and anomalous diffusion, and now, through our model, to neural oscillations.

Therefore, one of the possible linear models of cortical activity that satisfies all these three conditions can be represented using an MVAR model with colored innovations as follows:

$$\begin{aligned} \mathbf{j}_t &= \mathbf{j}_t^{\xi} + \mathbf{j}_t^{\alpha}, \\ \mathbf{j}_t^{\xi} &= (\mathbf{A} \circledast \mathbf{j}^{\xi})_t + \mathbf{u}_t^{\xi}, \\ \mathbf{j}_t^{\alpha} &= (\mathbf{A} \circledast \mathbf{j}^{\alpha})_t + \mathbf{u}_t^{\alpha}, \end{aligned} \tag{3}$$

where $(\mathbf{A} \circledast \mathbf{j})_t = \int_0^{\infty} \mathbf{A}_{\tau} \mathbf{j}_{t-\tau} \, d\tau$ denotes delayed convolution over interactions. The kernel $\mathbf{A}_{\tau} \in \mathbb{R}^{N_v \times N_v}$ is a delay-dependent matrix of autoregressive coefficients with a null diagonal, governing non-local spatiotemporal propagation between thalamocortical generators. The concatenation of these delay-dependent interactions forms the Delayed Connectome Tensor [25–27], which reflects the joint influence of anatomical connectivity and conduction delays. Petkoski and Jirsa [15] showed that incorporating delays qualitatively alters network dynamics, necessitating normalization of graph-theoretical metrics. To embed structural priors, we parametrize the convolution kernel through a spatiotemporal decomposition of interactions using a Hadamard product [25,28].

$$\mathbf{A}_{\tau} = \mathbf{C} \odot \delta(\tau - \mathbf{D}), \tag{4}$$

where $\delta(\cdot)$ is the Dirac delta function applied element-wise, and $\odot$ denotes the Hadamard (element-wise) product. The matrices $\mathbf{C} = w_C \, \bar{\mathbf{C}}$ and $\mathbf{D} = w_D \, \bar{\mathbf{D}}$ encode subject-specific coupling strengths and conduction delays, scaled from population-level priors $\bar{\mathbf{C}}$ and $\bar{\mathbf{D}} \in \mathbb{R}^{N_v \times N_v}$. Where w_D and w_C are structural modulatory weights that are selected within the search space, which warrant that the cortical activity represents a weakly stationary process and physiologically plausible values of conduction delays, respectively. This formulation links anatomical connectivity to dynamical interactions, in line with the framework proposed by Fukushima *et al.* [29]. The driven colored Gaussian noise process $\mathbf{u}_t^{\eta} \in \mathbb{R}^{N_v}$, with $\eta \in \{\xi, \alpha\}$, models the within thalamocortical unit dynamics for each spectral component as a collection of vertex-wise independent Hida-Matérn processes. Each process is zero-mean and temporally stationary, with autocovariance structure given by:

$$\mathbb{E}[\mathbf{u}_{t,i}^{\eta} \, \mathbf{u}_{t-\tau,k}^{\eta'}] = \delta_{i,k} \, \delta_{\eta,\eta'} \, \cos(2\pi F_i \tau) \, \mathcal{M}_i(\tau),$$

$$\mathcal{M}_i(\tau) = \frac{2\sqrt{\pi} A_i}{\sqrt{B_i} \, \Gamma(E_i)} \left(\frac{\pi|\tau|}{\sqrt{B_i}} \right)^{E_i - \frac{1}{2}} K_{E_i - \frac{1}{2}} \left(\frac{2\pi|\tau|}{\sqrt{B_i}} \right),$$

where $\delta_{i,k}$ and $\delta_{\eta,\eta'}$ are Kronecker deltas enforcing independence across vertices and SC, respectively (not to be confused with the Dirac delta function $\delta(\tau)$ used to describe autoregressive coefficients in the convolutional model). The function $\mathcal{M}_i(\tau)$ denotes the Matérn kernel shaping the temporal envelope. Here, $A_i > 0$ is the amplitude, $B_i > 0$ controls the temporal bandwidth (inversely related to peak sharpness), $E_i > \frac{1}{2}$ determines the smoothness, and $F_i \geq 0$ specifies the central frequency of oscillation. $K_{\nu}(\cdot)$ denotes the modified Bessel function of the second kind, and $\Gamma(\cdot)$ is the Euler Gamma Function [24].

As a result of this formulation, the corresponding power spectral densities of the aperiodic and α components at vertex i, $\mathbf{u}_{t,i}^{\xi}$ and $\mathbf{u}_{t,i}^{\alpha}$ coincide with the spectrum parameterization $\boldsymbol{\xi}_{\omega,i}$ and $\boldsymbol{\alpha}_{\omega,i}$ introduced by Pascual *et al.* [2,10].

$$\begin{aligned} \boldsymbol{\xi}_{\omega,i} &= \psi\left(\omega \mid A\xi_i,\, B\xi_i,\, E\xi_i,\, 0\right), \\ \boldsymbol{\alpha}_{\omega,i} &= \frac{1}{2}\psi\left(\omega \mid A\alpha_i,\, B\alpha_i,\, E\alpha_i,\, F\alpha_i\right) \\ &\quad + \frac{1}{2}\psi\left(\omega \mid A\alpha_i,\, B\alpha_i,\, E\alpha_i,\, -F\alpha_i\right), \end{aligned} \tag{5}$$

where the function $\psi(\omega \mid A, B, E, F)$ denotes a generalized Lorentzian spectral peak centered at frequency F, with amplitude A, bandwidth parameter B, and spectral exponent E (S3). These parameters fully determine the shape and scale of each generator's spectral profile (Fig. 1). Throughout this paper, we will refer to these quantities as the model's spectral parameters. In order to enforce sparsity over the SC, we will assume Group Lasso priors across the parameters of each cortical generator. This is done in order to ensure that if a given cortical generator does not contribute to a particular spectral component power (e.g., α or aperiodic), then all its corresponding spectral parameters are simultaneously driven to zero at the cortical generator [30].

As a consequence of this formulation, the ξ–αNET is a sparse, structurally constrained generative model of cortical activity in which each cortical vertex represents a lumped thalamo–cortical generator governed by coupled Hida–Matérn processes. Local dynamics are specified by the spectral parameters $\mathbf{A}\boldsymbol{\xi}$, $\mathbf{B}\boldsymbol{\xi}$, $\mathbf{E}\boldsymbol{\xi}$, $\mathbf{A}\boldsymbol{\alpha}$, $\mathbf{B}\boldsymbol{\alpha}$, $\mathbf{E}\boldsymbol{\alpha}$, $\mathbf{F}\boldsymbol{\alpha} \in \mathbb{R}^{N_v \times 1}$, which characterize the aperiodic (ξ) and oscillatory (α) components of the local power spectrum and implicitly capture thalamo–cortical dynamics. Long-range interactions are constrained by the structural parameters w_C and w_D, which modulate the strength and delays of cortico–cortical coupling. The model does not include an explicit thalamic representation; thalamic influences are embedded locally within the spectral parameters, while connectivity is exclusively cortico–cortical. Full mathematical details are provided in S1-S3.

Spectral Granger Causality

Within the ξ-αNET framework, the cortical activity of each spectral component is modeled as an independent MVAR process with Hida-Matérn innovations. This formulation implies that each spectral process defines an independent causal structure between cortical generators. Consequently, *spectral decomposition naturally entails a decomposition of effective connectivity*, in line with the decomposition of functional connectivity obtained using lagged coherence by Pascual *et al.* [10].

However, mapping effective connectivity within the ξ-αNET model cannot be done naively using standard measures such as Isolated Effective Coherence (iCoh), Lagged Coherence, Spectral Granger Causality (SGC), Partial Directed Coherence (PDC), or Noise Contribution Ratio (NCR) [16,31–34]. These connectivity measures assume temporally uncorrelated (white) innovations within the generative model. Therefore, in order to use them to map effective connectivity, it is necessary to express them in terms of the System Transfer Function (TF) of the generative of model in its innovation form or Wold representation [31,33]. In the case of the ξ-αNET model, each spectral component yields a frequency-resolved transfer function with explicit parametric expressions:

$$\mathbf{H}^{\xi}_{\omega,ik} = (\mathbf{I} - \mathbf{C} \odot \exp(-2\pi i\omega \mathbf{D}))^{-1}_{ik} \sqrt{\boldsymbol{\xi}_{\omega,k}},$$
$$\mathbf{H}^{\alpha}_{\omega,ik} = (\mathbf{I} - \mathbf{C} \odot \exp(-2\pi i\omega \mathbf{D}))^{-1}_{ik} \sqrt{\boldsymbol{\alpha}_{\omega,k}},$$

where $\mathbf{A}_\omega = \mathbf{C} \odot \exp(-2\pi i\omega\mathbf{D})$ denotes the frequency-resolved autoregressive coefficient matrix, incorporating structural connectivity and conduction delays. From these expressions, several key conclusions emerge. First, for directed propagation to occur from the source generator k into a target generator i, the spectral process must be active at the source generator (i.e., $\boldsymbol{\xi}_{\omega,k}$ or $\boldsymbol{\alpha}_{\omega,k}$ is nonzero) and also an anatomical path must exist between the source and target generators (i.e., $\mathbf{C}_{ik} \neq 0$). If $\boldsymbol{\xi}_{\omega,k}$ or $\boldsymbol{\alpha}_{\omega,k} \to 0$, then propagation is effectively suppressed. Second, each spectral process also defines a distinct cross-spectrum:

$$\mathbf{S}^{\xi}_{\omega} = \mathbf{H}^{\xi}_{\omega}\left(\mathbf{H}^{\xi}_{\omega}\right)^{\dagger}, \tag{6}$$

$$\mathbf{S}^{\alpha}_{\omega} = \mathbf{H}^{\alpha}_{\omega}\left(\mathbf{H}^{\alpha}_{\omega}\right)^{\dagger}. \tag{7}$$

From these spectral factorizations of the cross-spectra, we can compute the SGC to approximate the effective connectivity, as shown by Friston *et al.* [33] and Dhamala *et al.* [35], for each spectral process. By manipulating the cross-spectra of each spectral process, we derive an expression for the spectral power density at each generator:

$$\mathbf{S}_{\omega,ii} = \sum_{k=1}^{N_v} \left|(\mathbf{I} - \mathbf{A}_\omega)^{-1}_{ik}\right|^2 \left(\boldsymbol{\xi}_{\omega,k} + \boldsymbol{\alpha}_{\omega,k}\right). \tag{8}$$

Therefore, within the ξ-αNET framework, spectral power emerges as a consequence of network propagation, with the Green function $(\mathbf{I} - \mathbf{A}_\omega)^{-1}$ characterizing the redistribution of power across the network. In the limit of absent inter-generator coupling ($\mathbf{A}_\omega \to 0$), the model reduces to a purely local formulation, recovering the classical vertex-wise ξ-α model applied to the sources [2,3].

Bayesian Model Inversion

We estimate the parameters of ξ–αNET from rsEEG cross-spectral data in the `HarMNqEEG` dataset [36]. For each subject j, the model input is the empirical cross-spectrum $\mathbf{S}^{(j)} \in \mathbb{R}^{N_c \times N_c \times N_\omega}$, which represent the frequency-resolved sensor covariance. Parameter estimation is formulated as Maximum A Posteriori (MAP) estimation, combining the likelihood of the model-predicted source spectrum with priors on spectral and structural parameters (see S4). The closed analytical expression for the score function, Fisher Information Matrix, is discussed in S5 & S20.1, respectively.

The resulting MAP objective function is nonsmooth and non-convex, so we adopt a two-step profile likelihood strategy. First, the structural parameters for the connectivity and delay are estimated using Bayesian optimization, constrained by physiological priors from lifespan studies [37]. This defines subject-specific structural anchors. Second, spectral parameters are

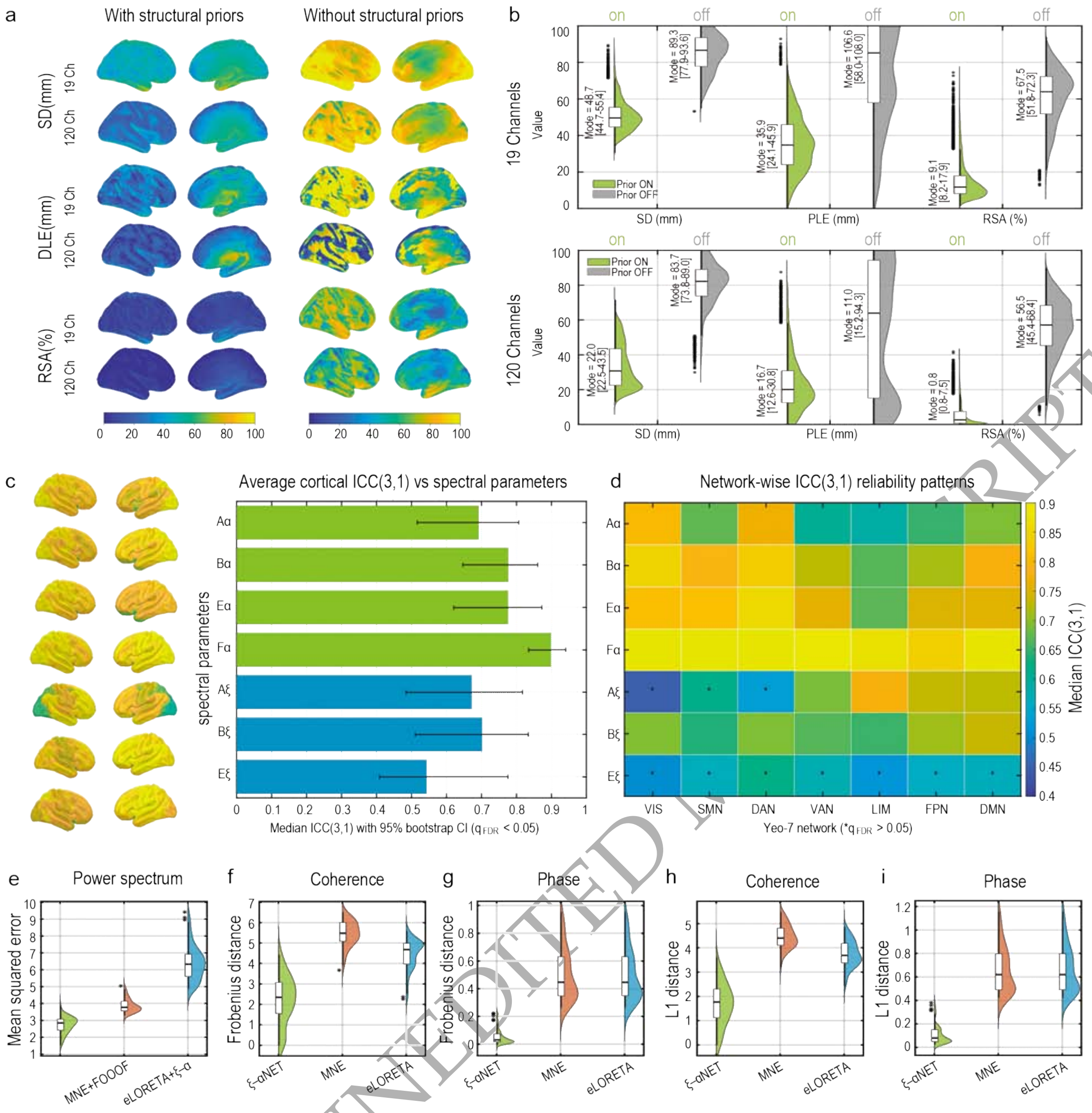

Figure 3. Benchmarking ξ–αNET. (a) Cortical maps of resolution–matrix metrics—spatial dispersion (SD), displacement/peak localization error DLE (i.e., PLE), and ratio of spurious activity (RSA)—computed from a linearization of the model *without* sparse priors (upper–bound estimates of spatial error). (b) Violin plots of SD, PLE, and RSA across 8003 voxels for 19– and 120–channel configurations; *green* = priors ON, *gray* = priors OFF. Priors substantially improve spatial identifiability, more than sensor count alone. Short–term test–retest reliability in an independent eyes–closed cohort (N = 60; two sessions 90 min apart, Ne = 19, Nv = 8003) (c). Median intraclass correlation coefficient (ICC(3,1)) is high for α parameters (≈0.70–0.86) and moderate for ξ parameters (≈0.45–0.70); among α features, *Peak Alpha Frequency* **F**α is most reliable. (d) Network–wise ICC shows high α reliability across all Yeo–7NET (Visual (VIS), Somatomotor (SMN), Dorsal Attention (DAN), Ventral Attention/Salience (VAN), Limbic (LIM), Frontoparietal Control (FPN), and Default Mode (DMN)) with a gradient peaking in sensory/attention systems; ξ parameters show relatively greater stability in frontal systems, with several networks not surviving FDR control. Benchmarking ξ–αNET model in source Cross-Spectrum Reconstruction from Neural-Mass Simulations (e–i). Neural–mass simulations (distinct from the ξ–αNET generative assumptions, Nsim = 100) show that ξ–αNET outperforms two–step pipelines (MNE+FOOOF and eLORETA+ξ–α) across power, coherence, and phase metrics, supporting the advantage of the model's one–step spectral inversion.

inferred using Stochastic FISTA with Nesterov acceleration [38], initialized from 50 random seeds within bounded domains. Model complexity is penalized using BIC, and regularization hyperparameters are tuned per subject via Bayesian optimization (note S4–S7).

Benchmarking ξ–αNET: identifiability with 19 electrodes, short–term reliability, and one–step superiority

We evaluate the identifiability and stability by (i) evaluating the analytical resolution matrix of a linearized ξ–αNET without sparsity priors (providing an upper bound on the spatial error of the full nonlinear estimator) and (ii) running ablations that remove structural priors. The results of this simulation are show in (Fig. 3a, b) and the full description of the methods is available in S9. Under these conditions, ξ–αNET attains macro-regional precision with 19 electrodes: PLE = 35.9 [24.1–45.9] mm, SD = 48.7 [44.7–55.4] mm, and RSA= 9.1 [8.2–17.9]% (Fig. 3b). These values lie within or near high-density EEG (hdEEG) reference ranges for methods reported by Hedrich *et al.* [39] of dSPM/MNE/sLORETA (PLE $\approx$ 25–40 mm; SD $\approx$ 35–45 mm; RSA $\approx$ 45–55%), while showing markedly lower RSA despite the lower sensor density. Using 120 electrodes further improves all metrics (PLE = 16.7 [12.6–30.8] mm; SD = 22.0 [22.5–43.5] mm; RSA = 0.8 [0.8–7.5]%), matching or surpassing hdEEG ranges from [39] ((Fig. 1) in S9). Removing the structural or delay priors degrades the performance, as shown in (Fig. 3a, b) (ΔPLE $\approx$ +70 mm, ΔSD $\approx$ +40 mm, ΔRSA $\approx$ +58%), indicating that structural priors substantially influence spatial identifiability beyond the sensor density alone.

We evaluated the impact of signal and channel noise on ξ–αNET by deriving the Fisher Information Matrix (S20.1), which shows that each sensor contributes an additive, negative correction proportional to its noise variance. Noisy channels, therefore, reduce likelihood curvature and increase posterior uncertainty under the Laplace approximation (S20.2). Parameter identifiability was quantified using Wald statistics from Laplace-approximated posteriors at the HCP-MMP1 level, corrected for multiple comparisons and summarized across Yeo 7 functional networks (Yeo–7NET) [40]. All parameters exhibited high and significant identifiability, indicating stable posterior solutions (S20.3).

We also assess short–term test–retest reliability on an independent open dataset ($N = 60$) with two eyes–closed sessions recorded 90 minutes apart, specifically collected for reliability studies [41–43] (Fig. 3c, d). Using this dataset, we inverted the ξ–αNET to estimate voxel-wise spectral parameters, which were then summarized across the Yeo-7NET. To estimate reliability we compute the intraclass correlation coefficient ICC(3,1) [44], estimate its bootstrap confidence intervals and use permutation test to evaluate the null hypothesis H_0 : ICC $\leq \rho_0$ at a conservative floor $\rho_0 = 0.40$ (poor–to–fair reliability), followed by Benjamini–Hochberg FDR control across parameters and networks (S10). We observed high short–term reproducibility for α–band parameters (median ICC $\approx$ 0.70–0.86), with peak alpha frequency $\mathbf{F}\boldsymbol{\alpha}$ (PAF) the most reliable; aperiodic ξ parameters showed moderate reliability (ICC $\approx$ 0.45–0.70). Network–wise, α spectral parameters are most reliable in sensory/attention systems (VIS, DAN, SMN), whereas ξ features were relatively more stable in frontal networks, with several non–sensory networks not surviving FDR (Fig. 3c, d). These results are consistent with [42], where α–band source reconstructions estimated with eLORETA showed the highest reliability, and lower reproducibility was reported for δ–band activity, which corresponds to the ξ process in our framework.

To benchmark accuracy while avoiding inverse–crime [45], we used 100 neural–mass simulations whose generative assumptions differ from ξ–αNET (S11). We then compared ξ–αNET (one–step joint inversion) to two two–step pipelines: MNE+FOOOF [6] and eLORETA+ξ–α. ξ–αNET achieved lower mean–squared error for source spectra and smaller Frobenius/L1 distances for coherence and phase, with tighter error distributions across runs (Fig. 3e–i). Gains in phase recovery specifically reflect the advantage of modeling conduction delays inside the inversion. These results align with the view that one-step inversion yields more accurate source estimates [17].

Together, these analyses show that ξ–αNET provides: (i) achieves spatial identifiability across 8,003 cortical vertices using 19 electrodes, further improved at 120, because anatomical and delay priors strongly constrain the solution; (ii) high short–term test–retest reliability, especially for α–band features [42]; and (iii) outperforms two-step pipelines in simulations designed to avoid model–mismatch biases (Fig. 3).

Spectral processes exhibit distinct cortical localizations and effective connectivity patterns across the Lifespan.

To map the distribution of SC and SGC or directed connectivity patterns of each spectral process across the Lifespan, we performed Bayesian model inversion of ξ-αNET on the HarMNqEEG dataset. For each subject j, the observed EEG cross-spectrum $\mathbf{S}^{(j)} \in \mathbb{R}^{N_c \times N_c \times N_\omega}$ was used to estimate individualized source-level SC via MAP optimization.

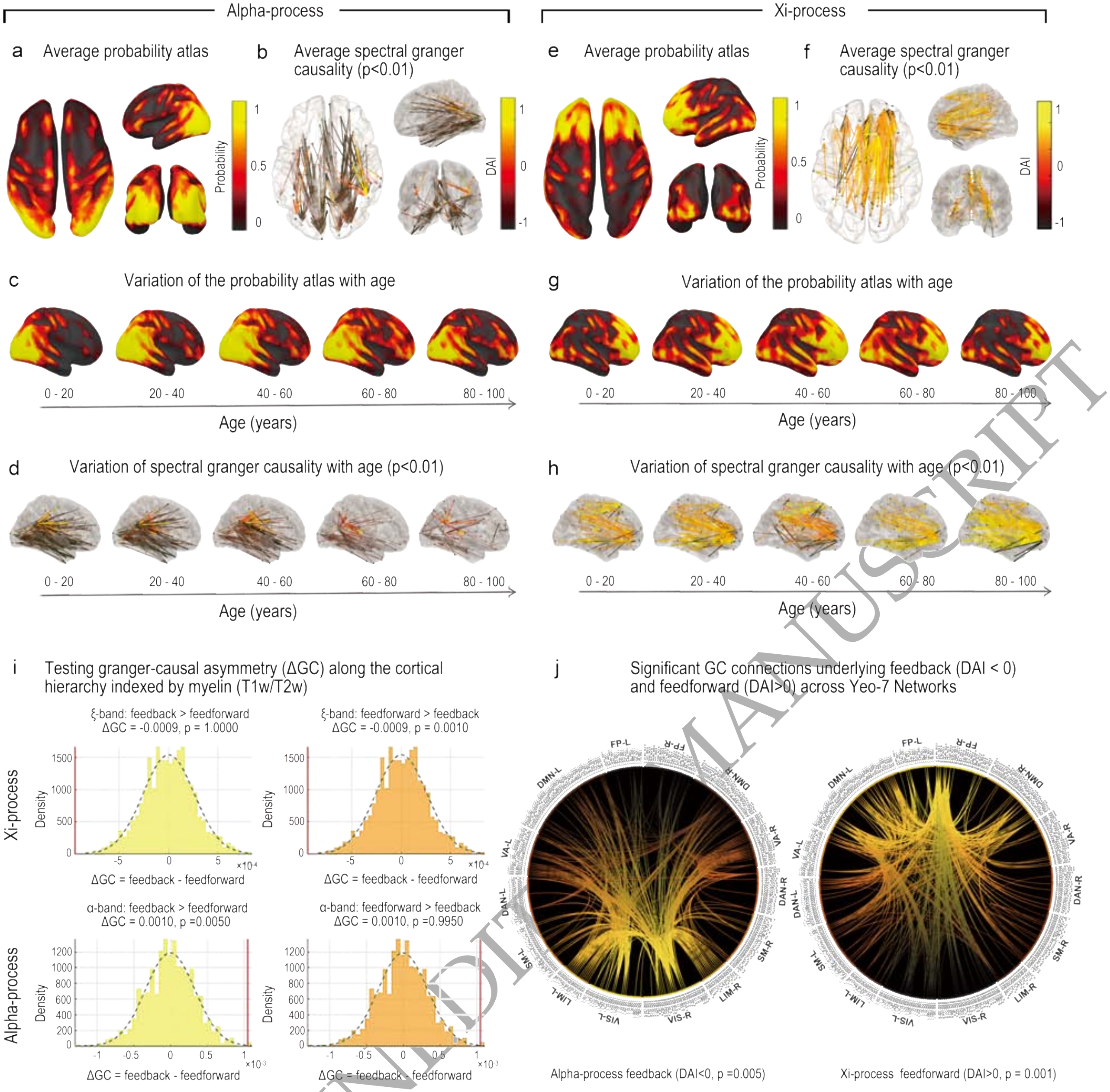

Figure 4. Lifespan Distribution of Probability atlas and Spectral Granger Causality for each Spectral Component. Effective connectivity across the lifespan, estimated with ξ–αNET on the HarMNqEEG dataset (N = 1965), reveals opposite directional networks for the α and ξ (aperiodic–delta) processes. (a–d) For the α-process, the Probability atlas, spectral Granger causality (Directional Asymmetry Index, DAI), and their lifespan variation are shown. (e–h) Analogous maps for the ξ-process. The α-process Probability atlas localizes mainly to posterior occipito-parietal cortices, whereas the ξ (aperiodic–delta) process exhibits more spatially dispersed sources with maxima over frontal and temporal regions. These spatial configurations remain consistent across the lifespan. The DAI (-1 = feedback, +1 = feedforward) was computed from the spectral Granger causality and referenced to the cortical myelination hierarchy (T1w/T2w). Across 1,965 participants, α-band connectivity consistently shows feedback dominance from frontal to posterior regions, whereas ξ-band connectivity remains feedforward, originating in sensory regions and projecting to higher-order networks throughout the lifespan. (i) Permutation tests show that Granger-causal (GC) values are significantly greater over feedback connections for the α-process and over feedforward connections for the ξ-process, given the approximate cortical myelination hierarchy ($p_{\alpha,\text{Feedback}} = 0.005$, $p_{\xi,\text{Feedforward}} = 0.001$). (j) Circular plots summarize significant directed connections within the Yeo-7NET: α-band feedback flows from frontoparietal and attentional hubs toward sensory systems, whereas ξ-band feedforward ascends from sensory and limbic regions toward frontoparietal and default-mode networks—demonstrating a clear double dissociation between feedback (α) and feedforward (ξ) signaling across the lifespan.

The localization probability of each SC over the cortex (Probability atlas), was estimated for each frequency bin and SC using the Nadaraya–Watson kernel density estimator over the amplitudes $\{\mathbf{A}\boldsymbol{\xi}^{(j)}, \mathbf{A}\boldsymbol{\alpha}^{(j)}\}_j$ across all subjects (S12). As shown in (Fig. 4a, c, e, g), the α-process

Probability atlas across the lifespan predominantly localizes to the posterior occipito-parietal region of the cortex. At the same time, the ξ (aperiodic–delta) process displays more spatially dispersed maxima over frontal and temporal cortices. To quantify directed interactions, we estimated frequency-resolved effective connectivity for both the α and ξ processes using the ξ–αNET spectral factorization (Eqs. 6-7) and the formulation of Dhamala *et al.* [35] to compute pairwise spectral Geweke–Granger causality, $\mathbf{G}_{\omega,j\to i}$. Vertex-wise causality values were summarized within the HCP–MMP1 parcellation [20], evaluating α at each subject's individual peak within the α band and ξ at its peak in the δ range. Group-level SGC matrices were then obtained by averaging within age bins and across the full cohort (Fig. 4b, d, f, h). The statistical significance of directed connections was assessed through 5,000 joint permutations of the group-mean matrix under a spatial null model ($\alpha = 0.01$). Feedforward and feedback directions were defined according to the approximate cortical hierarchy gradient derived from myelination (T1w/T2w) values as shown by Burt *et al.*, [46]. For each spectral process and age bin, we computed the Directional Asymmetry Index (DAI) following Bastos *et al.* [47], weighting its sign by the cortical-myelination gradient so that positive values represent feedforward and negative values feedback connectivity (note S13).

Permutation tests of Granger-causal asymmetry revealed that α-process connectivity is significantly stronger over feedback pathways ($p_{\alpha,\text{Feedback}} = 0.005$), whereas ξ-process connectivity is stronger over feedforward pathways ($p_{\xi,\text{Feedforward}} = 0.001$) (Fig. 4i). Finally, circular graphs summarizing significant directed connections within the Yeo-7NET [40] (Fig. 4j) were constructed from the DAI-filtered adjacency matrices, selectively displaying only those connections whose directionality (feedforward for ξ; feedback for α) was found to be significant in the permutation test. Networks are arranged from sensory (bottom) to frontal (top) order, approximately according to the cortical myelination hierarchy (S13).

In the left panel of Fig. 4j, the α-process shows feedback-dominated connectivity, with edges converging from higher-order frontoparietal (FP), dorsal attention (DAN), and default-mode (DMN) networks toward visual (VIS) and somatomotor (SMN) networks. This top-down pattern reflects inhibitory and attentional control from the executive to the sensory systems, with the strongest feedback along the FP ↔ DAN/DMN and DAN ↔ VIS pathways. Conversely, in the right panel, the ξ (aperiodic–delta) process exhibits feedforward-dominated connectivity, originating in sensory and limbic (LIM) regions and projecting toward FP and DMN networks. Prominent VIS → DAN/FP and SMN/LIM → DMN links indicate ascending broadband drive from perceptual and subcortical areas to higher-order regions. Together, these patterns reveal a clear double dissociation between feedback α and feedforward ξ processes, consistent with hierarchical models of neural oscillations [47,48].

Finally, we performed a cross-dataset replication to confirm the robustness of these findings. As shown in (Fig. 2 in S10), the model inverted on two independent datasets—a test–retest cohort ($N = 60$, first two sessions) [41–43] and the large-scale HarMNqEEG dataset—yielded highly consistent spatial Probability atlases, reflecting nearly identical cortical localization gradients ($r > 0.9$, $P_{\text{spin}} < 0.01$, computed using the Neuromaps plugin in `Brainstorm`). Directed connectivity patterns were qualitatively preserved, with the α-process exhibiting predominantly feedback and the ξ-process predominantly feedforward organization.

Spectral Components localization correlates with significant inverted U-Shape developmental trajectories and an increase in localization probability

ξ-αNET inversion yields, for each subject j, vertex-wise estimates of spectral amplitude for both the aperiodic component $\mathbf{A}\boldsymbol{\xi}^{(j)}$ and the α-band component $\mathbf{A}\boldsymbol{\alpha}^{(j)}$, as well as the corresponding PAF map $\mathbf{F}\boldsymbol{\alpha}^{(j)}$. While age-related changes in these features have been widely reported at the sensor level [36,49–51], their spatially resolved trajectories at the cortical source level have not been systematically characterized across the Lifespan.

Due to the assumption of Group Lasso priors on the generative model of the ξ-αNET, the distributions of $\mathbf{A}\boldsymbol{\xi}^{(j)}$, $\mathbf{A}\boldsymbol{\alpha}^{(j)}$, and $\mathbf{F}\boldsymbol{\alpha}^{(j)}$ are inherently sparse, with many vertices exhibiting exact zeros. The resulting execs of zeros in the data its known as zero inflation, which violates key assumptions of conventional Gaussian-based regression. Therefore, to map the developmental trajectories of the SC accurately, we employed a Zero-Inflated Gaussian (ZIG) regression model. The use of this type of regression model enables us to account for sparsity, non-negativity, and nonlinear age effects, providing a robust statistical basis for mapping developmental trends in

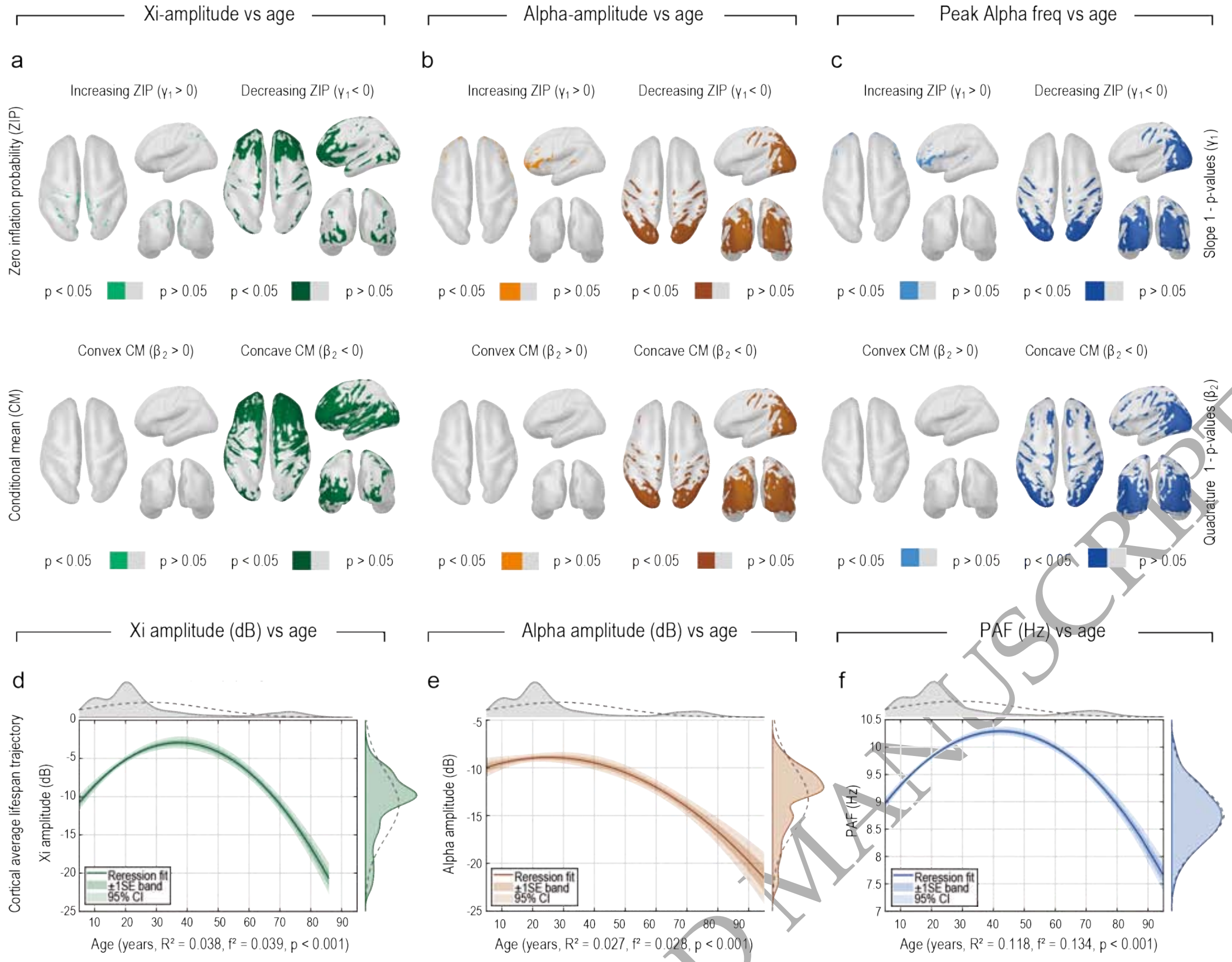

Figure 5. Developmental Atlas of spectral EEG components estimated with zero-inflated Gaussian (ZIG) regression on HarMNqEEG (N=1965). All panels use vertex-wise ZIG models that jointly estimate the zero-inflation probability (ZIP) and the conditional mean (CM) as functions of age. Maps display significance masks (p<0.05) for two distinct effects: (i) the age slope γ_1 of the ZIP component (change in zero-inflation with age; coloured = significant, grey = not significant), and (ii) the age quadratic curvature β_2 of the CM component (concavity/convexity of the nonzero mean trajectory with age). (a) ξ-amplitude ($\mathbf{A}\xi$): ZIP decreases widely with age ($\gamma_1 < 0$), indicating more frequent detectability; CM shows predominantly concave (inverted-U) trajectories ($\beta_2 < 0$) with wide spread cortical distribution. (b) α-amplitude ($\mathbf{A}\alpha$): ZIP increases mainly in the frontal cortex and decreases in the occipital cortex, revealing an anterior–posterior gradient; CM curvature is largely concave posteriorly, consistent with growth in early–mid adulthood followed by decline. (c) Peak α frequency (PAF; $\mathbf{F}\alpha$): using the same ZIG formulation, maps show negative age slopes predominantly in posterior regions ($\gamma_1 < 0$) and concave CM curvature concentrated occipitally ($\beta_2 < 0$), consistent with a lifespan slowing most pronounced in posterior cortex. (d-f) Cortical-average trajectories (density plots; robust quadratic regression): $\mathbf{A}\xi$, $\mathbf{A}\alpha$, and $\mathbf{F}\alpha$ show statistically significant inverted-U patterns across the lifespan; effect sizes are small for amplitudes and larger for PAF (panel labels report R^2 and f^2; all p<0.001). For each trajectory, both 95% confidence bands and ±1 SE envelopes are shown.

source-resolved spectral activity [52].

We employed a vertex-wise ZIG regression model of the form (S14):

$$\begin{aligned} Y_{ij} &\sim \mathrm{ZIG}\left(\mu_{ij}, \sigma^2_{ij}, \pi_{ij}\right), \\ \mu_{ij} &= \beta_{0,i} + \beta_{1,i} a_j + \beta_{2,i} a_j^2, \\ \mathrm{logit}\left(\pi_{ij}\right) &= \gamma_{0,i} + \gamma_{1,i} a_j, \end{aligned} \tag{9}$$

where Y_{ij} denotes the response variable—either $\mathbf{A}\xi$, $\mathbf{A}\alpha$, or $\mathbf{F}\alpha$—in vertex i for subject j, and a_j is the subject's age. On the other hand, the function $\mathrm{logit}(p) = \log\left(p/(1-p)\right)$ is the logit link, and μ_{ij} is the conditional mean (CM) which captures the expected value of the positive (non-zero) portion of the distribution.

(Fig. 5) presents the developmental atlas of spectral EEG components estimated with zero-inflated Gaussian (ZIG) regression applied to the main spectral parameters of the ξ–αNET model across the full HarMNqEEG dataset. Each vertex-wise ZIG model jointly estimated the ZIP and the CM as smooth functions of age, thereby disentangling effects related to the detectability of spectral components from those governing their nonzero amplitudes.

Panels 5(a)–(c) display significance maps ($p < 0.05$) for two age effects: the ZIP slope (γ_1, top row) indicating how the probability of zero inflation changes with age, and the CM quadratic curvature (β_2, bottom row) reflecting whether the nonzero mean follows a convex or concave (inverted-U) trajectory.

For the $\mathbf{A}\boldsymbol{\xi}$ amplitude (Fig. 5a), ZIP decreases widely with age ($\gamma_1 < 0$), meaning that aperiodic ξ activity becomes increasingly detectable across the cortex in older individuals. The CM component exhibits predominantly concave trajectories ($\beta_2 < 0$), indicating that $\mathbf{A}\boldsymbol{\xi}$ follows a trajectory of growth and decline. The $\mathbf{A}\boldsymbol{\alpha}$ amplitude (Fig. 5b) reveals a pronounced anterior–posterior gradient: ZIP increases in frontal areas but decreases occipitally, suggesting reduced detectability of α rhythms in anterior cortex with age. The CM curvature remains concave in posterior regions ($\beta_2 < 0$), consistent with growth through early-to-mid adulthood followed by decline in regions generating α oscillations. For the peak α frequency ($\mathbf{F}\boldsymbol{\alpha}$; PAF) (Fig. 5c), ZIP slopes are predominantly negative in posterior cortex ($\gamma_1 < 0$), while CM curvature is concave and confined to occipital areas ($\beta_2 < 0$), consistent with a lifespan slowing of PAF most pronounced in posterior regions. Finally, (Fig. 5d, e, f) summarizes cortical-average lifespan trajectories using robust quadratic regression. All three spectral variables—$\mathbf{A}\boldsymbol{\xi}$, $\mathbf{A}\boldsymbol{\alpha}$, and $\mathbf{F}\boldsymbol{\alpha}$—exhibit statistically significant inverted-U patterns (all $p< 0.001$), with small effect sizes for amplitudes and larger ones for PAF.

Together, these findings demonstrate that both aperiodic and α EEG components follow non-monotonic developmental trajectories that differ spatially across the cortex. The results replicate and extend canonical sensor-level observations of PAF lifespan slowing to the source level, revealing that the posterior–anterior gradient in ZIP modulates where α activity remains detectable. Overall, the localization of spectral components correlates with significant inverted-U developmental trajectories.

Estimated Conduction Delays are negatively correlated with the Peak Alpha Frequency and with independently reported cortical myelin (T1w/T2w) data

Conduction delays are governed by axonal diameter and myelin thickness, which jointly determine the velocity of action potential propagation along white-matter tracts. Myelination—the ensheathing of axons by lipid-rich membranes—enhances conduction speed and exhibits a characteristic non-monotonic trajectory across the lifespan: it increases from childhood through early adulthood, plateaus in midlife, and declines with aging, yielding an inverted-U pattern of cortical myelin content [53,54]. This trajectory, consistently observed in T1w/T2w MRI studies, modulates conduction velocity and the temporal synchronization of neural activity. In line with the Rushton model [55], myelin thickness scales inversely with the square of mean conduction delay ($\propto 1/\langle\tau\rangle^2$). We therefore defined an EEG-based *myelination proxy* as $1/\langle\tau\rangle^2$, expected to reproduce the same inverted-U lifespan trajectory.

To test this electrophysiological prediction, we estimated conduction delays in 1,965 participants from the HarMNqEEG dataset using the ξ–αNET model. For each participant j, the mean conduction delay $\langle\tau\rangle^{(j)}$ was obtained by averaging the estimated delay matrix across all neurotracts ($\langle\tau\rangle^{(j)} = \sum_i \sum_k \mathbf{D}_{ik}^{(j)}$), and the corresponding myelination proxy was defined as $1/(\langle\tau\rangle^{(j)})^2$ (note S15). Lifespan trajectories were modeled as functions of age a_j using eight piecewise cubic B-spline basis functions, with optimal smoothing selected via AIC, following Grydeland et al. [53]. The significance of quadratic curvature was assessed using robust quadratic regression. The resulting trajectory revealed a pronounced U-shaped pattern of conduction delays across the lifespan ($p_{\text{quad}} = 1.75 \times 10^{-63}$), marked by rapid acceleration in early development, stabilization in midlife, and slowing in older age (Fig. 6a).

To compare the electrophysiological myelination proxy with independent MRI-derived measures, we used the cortical T1w/T2w myelination dataset from Grydeland et al. [53] ($N = 484$), also reported in Fig. 4a of de Faria et al. [54]. Both the EEG-based proxy and the MRI-derived myelin measure were z-score normalized prior to modeling. The EEG-derived proxy showed a significant inverted-U lifespan trajectory ($p_{\text{quad}} = 2.14 \times 10^{-9}$), while the MRI curve exhibited $R^2_{\text{myelin}} = 0.611$ and $f^2_{\text{myelin}} = 1.57$. The correlation between the two spline trajectories was high ($\rho = 0.95$), indicating strong convergence of their developmental patterns (Fig. 6b). However, the EEG-derived proxy displayed wider 95% confidence intervals and a smaller effect size ($R^2 = 0.121$, $f^2 = 0.137$), reflecting the higher noise inherent to electrophysiological estimates compared with MRI-based myelin measurements.

The first derivatives of the spline fits—reflecting myelinogenesis rates—for both cortical myelination and the electrophysiological myelination proxy followed qualitatively similar

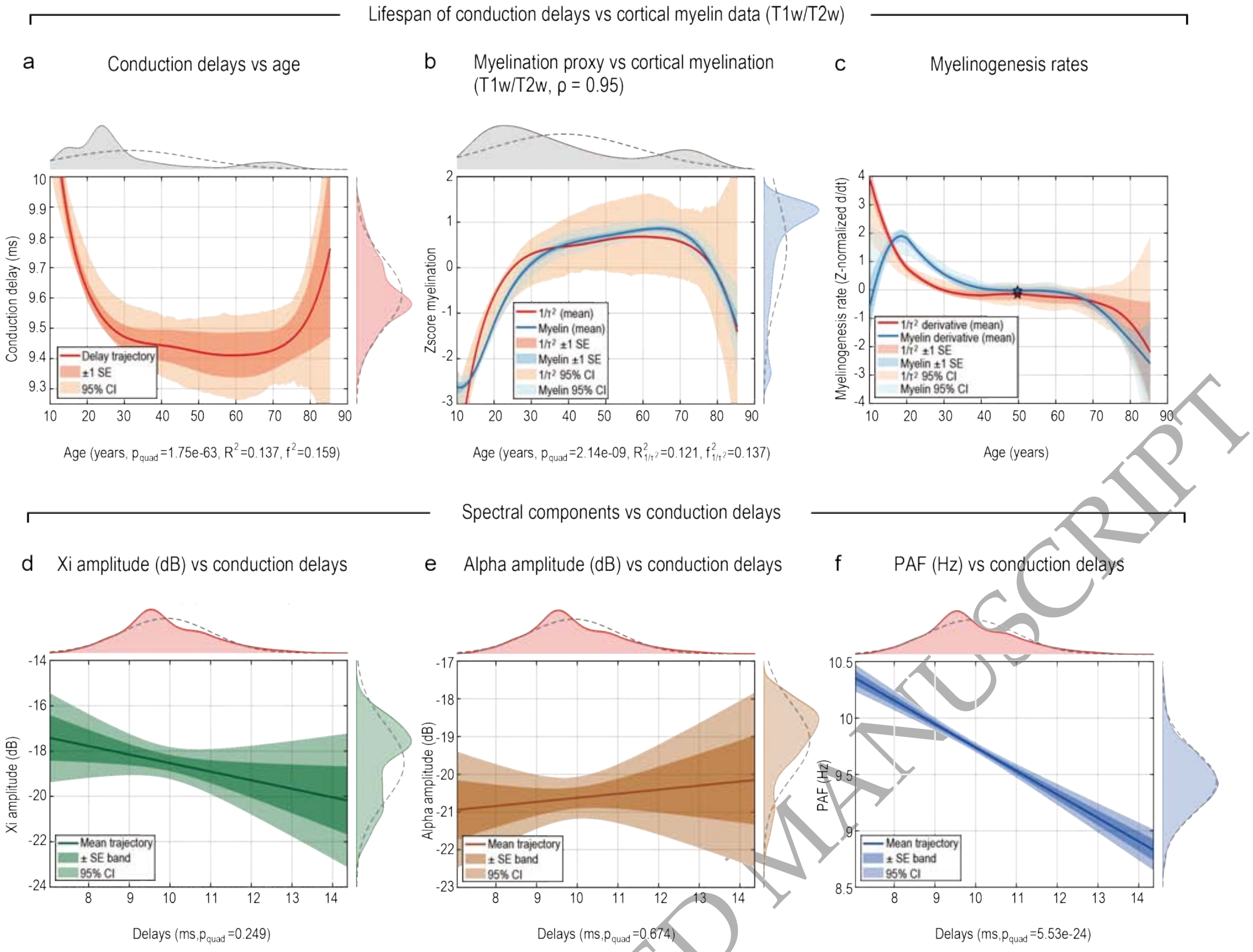

Figure 6. Lifespan dynamics of conduction delays, cortical myelination, and spectral components. Lifespan trajectories were estimated using eight piecewise cubic B-spline basis functions, with smoothing parameters selected via AIC minimization. (a) Mean conduction delays estimated by ξ–αNET across the HarMNqEEG dataset ($N = 1965$) show a U-shaped trajectory with age ($p_{\text{quad}} = 1.75 \times 10^{-63}$, estimated fitting a robust quadrtic model). (b) Z-scored myelination proxy ($1/\text{Delay}^2$, orange) and empirical cortical myelination (T1w/T2w, blue) from Grydeland *et al.* [53] ($N = 484$) exhibit highly correlated inverted-U trajectories ($\rho = 0.95$), with $R^2_{\text{myelin}} = 0.611$ and $f^2_{\text{myelin}} = 1.570$. (c) First derivatives of spline fits (myelinogenesis rates) converge near 50 years, marking midlife stabilization of cortical myelination. (d–f) Associations between conduction delays and spectral parameters: only $\mathbf{F}\alpha$ (PAF) declines declines significative with increasing delays ($p = 5.53 \times 10^{-24}$).

trajectories for ages above 15 years. In both cases, the rate approached zero around 50 years of age, indicating the midlife stabilization of cortical myelination consistently reported in MRI studies and mirrored by our proxy (Fig. 6c). Minor discrepancies at younger ages likely arise from spline boundary effects, the nonlinear relationship between true myelin content and its proxy (Myelin $\sim A(1 - \exp(-B/\tau^2))$, where $1/\tau^2$ is a first-order Taylor approximation), and the greater noise inherent to EEG-derived conduction delays compared with MRI-based measures.

Regression analyses further revealed a significant negative relationship between conduction delays and the peak alpha frequency ($\mathbf{F}\alpha$, $p = 5.53 \times 10^{-24}$). In contrast, neither $\mathbf{A}\xi$ ($p = 0.25$) nor $\mathbf{A}\alpha$ ($p = 0.67$) showed significant associations (Fig. 6d, e, f). Faster conduction—reflecting higher myelin content—was thus linked to higher $\mathbf{F}\alpha$ values, supporting the view that alpha-rhythm frequency depends on axonal conduction efficiency. This finding aligns with earlier observations that diffusion-tensor-derived fractional anisotropy correlates with PAF in the Cuban Human Brain Mapping Project [56] and with theoretical predictions from thalamocortical modeling [21,22,57], where conduction delays govern the emergence of oscillatory alpha modes.

Together, these results demonstrate that ξ–αNET can infer physiologically meaningful conduction delays from resting-state EEG. The inferred trajectories parallel those of cortical myelination measured by MRI and reveal a tight structural–functional coupling whereby white-matter integrity constrains the spectral dynamics of cortical rhythms. The strong inverse relationship between $\mathbf{F}\boldsymbol{\alpha}$ and conduction delay highlights PAF as a sensitive functional marker of myelin-dependent transmission speed across the human lifespan.

Conclusion and Discussion

We introduce ξ–αNET, a generative model of EEG cortical activity that represents each spectral component as a sparse, structurally constrained network of independent Hida–Matérn processes in the time domain. By integrating the sparse connectome derived from dMRI [58] and conduction delays estimated from CCEP [37], the model captures the spatiotemporal dependencies among cortical generators and yields Lorentzian spectral profiles describing spectral processes that reduce, in the limit without priors, to the traditional SCM framework of Pascual *et al.* [2,10,56,59]. This framework unifies spectral decomposition and effective connectivity mapping while explicitly incorporating anatomical and delay priors in the generative model—an aspect neglected in existing SCM approaches [6,9,10]. Analyses demonstrate that ξ–αNET achieves good spatial resolution, high short-term test–retest reliability—especially for α rhythm features [42]—and superior accuracy over standard two-step pipelines in simulations controlling for model-mismatch biases (Fig. 3).

Using Bayesian inversion, ξ–αNET revealed distinct lifespan trajectories and directional architectures for the ξ (aperiodic–delta) and α processes across the HarMNqEEG. The ξ component exhibited widespread cortical engagement and a predominant feedforward organization, under the cortical myelination hierarchy of Burt *et al.* [46], with ascending influences from sensory to higher-order regions. In contrast, the α-rhythm localized to posterior cortices and exhibited a feedback organization across development, consistent with the pattern described by Michalareas *et al.* [48] (Fig. 4). Both α-amplitude and PAF followed inverted U-shaped age trajectories, reflecting maturation and later slowing of cortical feedback loops consistent with previous empirical and theoretical results (Fig. 5). Conduction-delay estimates are negatively correlated with the PAF, as suggested by previous empirical and theoretical studies [21,56,57].

Additionally, conduction delays closely mirrored empirical cortical myelination (T1w/T2w) from Grydeland *et al.* [53], exhibiting highly correlated inverted-U trajectories across the lifespan. The first derivatives of these spline fits—representing myelinogenesis rates—showed similar age-dependent patterns, approaching zero around midlife, marking the stabilization of cortical myelination observed in MRI studies and reflected in our electrophysiological proxy (Fig. 6).

We believe that a unified generative framework for spectral component modeling is necessary to explain how different spectral processes arise within realistic brain networks and how they give rise to effective connectivity patterns grounded in anatomy across the lifespan. By jointly estimating structural and spectral parameters while incorporating structural priors, this approach aims to bridge the gap between structure, dynamics, and function. In doing so, it moves beyond merely descriptive analyses and provides a pathway for using EEG to investigate how processes such as myelination may regulate spectral dynamics. We expect that individually estimated ξ–αNET parameters can be used to identify biomarkers of different neurological conditions. As illustrated by the Parkinson's disease analysis in S21, subject-level estimates reveal disease-related alterations in spectral dynamics in a concrete clinical setting, specifically showing a slowing of the alpha rhythm in Parkinson's subjects relative to age-matched controls from HarMNqEEG. Building on this proof of concept, future work will focus on constructing normative reference datasets to enable systematic detection, quantification, and interpretation of patient-specific deviations from the norm in a clinically meaningful framework.

The ξ–αNET framework has several limitations. Its reduction of thalamocortical dynamics and cortico-cortical interactions to a linear MVAR model with colored Hida–Matérn innovations cannot capture the nonlinear excitatory–inhibitory interactions, attractor dynamics, and state-dependent transitions that characterize real cortical activity. Incorporating nonlinear activation functions could improve biological realism. The use of a Dirac delta function to represent conduction delays also oversimplifies temporal dispersion, which may be better modeled using broader delay distributions such as the exponential family [25]. Furthermore, our analyses relied on low-density EEG, which limits its spatial resolution compared with high-density recordings or MEG. Although the model can, in principle, be extended to MEG by changing the lead field, this has not yet been tested.

The present work also focuses exclusively on two spectral components—the aperiodic (ξ) and α processes—without assessing the role or directionality of higher-frequency rhythms, such as gamma, which may critically contribute to feedforward signaling. Finally, the current formulation assumes stationarity, which restricts its applicability to transient or task-related dynamics [7]. Addressing these limitations, including nonlinear modeling, richer delay priors, higher-density data, and extended spectral coverage, will be essential to further enhance ξ–αNET's generality and biological fidelity.

Materials and Methods

Resources and Code

All analyses were performed on a high-performance server (52 CPUs, 256 GB RAM). The full ξ–αNET pipeline, including parameter estimation, visualization, regression, and documentation, is available on GitHub (`Xi-AlphaNET`). Reproducibility resources (commit and tag, MATLAB environment file, and minimal scripts for every figure and statistic) are detailed in S19.

Data

Both structural and electrophysiological data informed the model. Structural priors were derived from the anatomical connectivity $\bar{\mathbf{C}}$ of Rosen *et al.* [58] or in `Zenodo`, and the axonal conduction-delay $\bar{\mathbf{D}}$ from the `F-TRACT` consortium, estimated using CCEP [37]. The head model, source model, and lead-field matrix were obtained using the `Ciftistorm`–Brainstorm pipeline implemented on the *fsaverage* cortical surface (N_v = 8003 vertices) [60]. Empirical data were taken from the `HarMNqEEG` dataset [36], which provides resting-state EEG cross-spectral tensors (N_c = 19, N_ω = 47) from 1,965 participants aged 5–100 years across nine countries, as well as from the short-term test–retest dataset [41–43]. Preprocessing followed the procedures described by Li *et al.* [36], including average referencing, removal of global scaling, and cross-spectral regularization (S17–S18). Cortical myelination (T1w/T2w) values were obtained from the Human Connectome Project (S1200 release) and summarized over the HCP–MMP1 parcellation using `Neuromaps`. In addition, the raw cortical myelination dataset (N = 484) from Grydeland *et al.* [53] was used to estimate myelination and myelinogenesis trajectories and was compared with our EEG-based myelination proxy.

All ξ–αNET-derived spectral and structural parameters from HarMNqEEG are publicly available (`Xi-AlphaNET Data`, ~ 60 GB). The repository includes source power spectra, cross-spectral matrices, cortical activation and connectivity maps, conduction delay matrices, and all structural priors necessary to reproduce the results for both the HarMNqEEG [36] and test-retest dataset [42,61]. A graphical interface for visualization is provided within the Xi-AlphaNET app.

FUNDING

This work was supported in part by the STI 2030 – Major Projects (2022ZD0208500); the National Natural Science Foundation of China (W2411084); the Key Research and Development Projects of the Science and Technology Department of Chengdu (2024-YF08-00072-GX); and the Chengdu Science and Technology Bureau Program (2022-GH02-00042-HZ). Additional support was provided by the University of Electronic Science and Technology of China (UESTC) through the CNS Program (Y0301902610100201). This work was also supported by funding from the European Union's Horizon Europe Programme under the Specific Grant Agreements No. 101147319 (EBRAINS 2.0 Project) and No. 101137289 (Virtual Brain Twin Project), as well as by a government grant managed by the Agence Nationale de la Recherche (ANR) under the France 2030 program (ANR-22-PESN-0012). L.M. gratefully acknowledges personal support from the Hundred Talents Program of UESTC, the Outstanding Young Talents Program (Overseas) of the National Natural Science Foundation of China, and talent programs of Sichuan Province and Chengdu Municipality.

ACKNOWLEDGMENTS

We thank the anonymous reviewers for their constructive feedback, which greatly improved the quality and rigor of this manuscript. We also express our gratitude to the group of Grydeland et al. [53] for sharing the raw cortical myelination dataset that enabled the estimation of myelination and myelinogenesis trajectories.

AUTHOR CONTRIBUTIONS

R.G.R., L.M., and P.A.V.S. conceived and designed the study. R.G.R., P.A.V.S., and A.A.G. developed the Xi-AlphaNET software and visualization interface. R.G.R. conducted the formal analysis and wrote the original draft. L.M., C.L., P.X., D.Y., V.J., and M.L.B.V. contributed substantially to the interpretation and discussion of the results. R.G.R., Y.W., Y.J., and A.A.G. prepared visualizations. S.Y. participated in the review of the bibliography. M.L.B.V., C.L., P.X., D.Y., V.J., and L.M. contributed to the manuscript review and editing. P.A.V.S. and L.M. supervised the project. P.A.V.S., L.M., V.J., and C.L. acquired funding for the research.

CONFLICT OF INTEREST

None declared.

REFERENCES

1. Zetterberg LH. Estimation of parameters for a linear difference equation with application to eeg analysis. *Math Biosci* 1969; **5**: 227–75.
2. Pascual-Marqui RD, Valdes-Sosa PA and Alvarez-Amador A. A parametric model for multichannel eeg spectra. *Int J Neurosci* 1988; **40**: 89–99.
3. Valdes P, Bosch J, Grave R *et al.* Frequency domain models of the eeg. *Brain Topogr* 1992; **4**: 309–19.
4. Whitten TA, Hughes AM, Dickson CT *et al.* A better oscillation detection method robustly extracts eeg rhythms across brain state changes: the human alpha rhythm as a test case. *Neuroimage* 2011; **54**: 860–74.
5. Wen H and Liu Z. Separating fractal and oscillatory components in the power spectrum of neurophysiological signals. *Brain Topogr* 2016; **29**: 13–26.
6. Donoghue T, Haller M, Peterson EJ *et al.* Parameterizing neural power spectra into periodic and aperiodic components. *Nat Neurosci* 2020; **23**: 1655–65.
7. Wilson LE, da Silva Castanheira J and Baillet S. Time-resolved parameterization of aperiodic and periodic brain activity. *eLife* 2022; **11**: e77348.
8. Brady B and Bardouille T. Periodic/aperiodic parameterization of transient oscillations (papto)–implications for healthy ageing. *Neuroimage* 2022; **251**: 118974.
9. Hu S, Zhang Z, Zhang X *et al.* Xi-pi: a nonparametric model for neural power spectra decomposition. *IEEE J Biomed Health Inform* 2024; **28**: 2624–35.
10. Pascual-Marqui RD, Kochi K and Kinoshita T. Cortical xi-alpha model for resting state electric neuronal activity. *arXiv* 2022; arXiv:2212.13571.
11. Miller KJ, Sorensen LB, Ojemann JG *et al.* Power-law scaling in the brain surface electric potential. *PLoS Comput Biol* 2009; **5**: e1000609.
12. He BJ. Scale-free brain activity: past, present and future. *Trends Cogn Sci* 2014; **18**: 480–7.
13. Alvarez-Amador A, Valdes-Sosa PA, Pascual-Marqui RD *et al.* On the structure of eeg development. *Electroencephalogr Clin Neurophysiol* 1989; **73**: 10–19.
14. Jirsa VK. Neural field dynamics with local and global connectivity and time delay. *Phil Trans R Soc A* 2009; **367**: 1131–43.
15. Petkoski S and Jirsa VK. Transmission time delays organize the brain network synchronization. *Phil Trans R Soc A* 2019; **377**: 20180132.
16. Garcia Reyes R and Valdes-Sosa PA. Mapping effective connectivity. *Reference module in neuroscience and biobehavioral psychology*, (Elsevier2025).
17. Paz-Linares D, Gonzalez-Moreira E, Areces-Gonzalez A *et al.* Minimizing the distortions in electrophysiological source imaging of cortical oscillatory activity via spectral structured sparse bayesian learning. *Front Neurosci* 2023; **17**: 978527.
18. Feng J, Jirsa V and Lu W. Human brain computing and brain-inspired intelligence. *Natl Sci Rev* 2024; nwae144.
19. Lu W, Zeng L, Wang J *et al.* Imitating and exploring the human brain's resting and task-performing states via brain computing: scaling and architecture. *Natl Sci Rev* 2024; **11**: nwae080.
20. Glasser MF, Coalson TS, Robinson EC *et al.* A multi-modal parcellation of human cerebral cortex. *Nature* 2016; **536**: 171–8.
21. Robinson PA, Loxley PN, O'Connor SC *et al.* Modal analysis of corticothalamic dynamics, electroencephalographic spectra, and evoked potentials. *Phys Rev E* 2001; **63**: 041909.
22. Robinson PA, Whitehouse RW and Rennie CJ. Nonuniform corticothalamic continuum model of electroencephalographic spectra with application to split-alpha peaks. *Phys Rev E* 2003; **68**: 021922.
23. Lilly JM, Sykulski AM, Early JJ *et al.* Fractional brownian motion, the matérn process, and stochastic modeling of turbulent dispersion. *Nonlinear Process Geophys* 2017; **24**: 481–514.
24. Dowling M, Sokół P and Park IM. Hida-matérn kernel. *arXiv* 2021; arXiv:2107.07098.
25. Gonzalez Mitjans A, Paz Linares D, Lopez Naranjo C *et al.* Accurate and efficient simulation of very high-dimensional neural mass models with distributed-delay connectome tensors. *Neuroimage* 2023; **274**: 120137.
26. Karahan E, Rojas-Lopez PA, Bringas-Vega ML *et al.* Tensor analysis and fusion of multimodal brain images. *Proc IEEE* 2015; **103**: 1531–59.
27. Reyes RG and Martinez Montes E. Modeling neural activity in neurodegenerative diseases through a neural field model with variable density of neurons. *bioRxiv* 2022; 2022–08.
28. Greaves MD, Novelli L, Mansour SL *et al.* Structurally informed models of directed brain connectivity. *Nat Rev Neurosci* 2024; 1–19.
29. Fukushima M, Yamashita O, Knösche TR *et al.* Meg source reconstruction based on identification of directed source interactions on whole-brain anatomical networks. *Neuroimage* 2015; **105**: 408–27.
30. Friedman J, Hastie T and Tibshirani R. A note on the group lasso and a sparse group lasso. *arXiv* ; arXiv:1001.0736.
31. Pascual-Marqui RD, Biscay RJ, Bosch-Bayard J *et al.* Isolated effective coherence (icoh): causal information flow excluding indirect paths. *arXiv* 2014; arXiv:1402.4887.
32. Valdes-Sosa PA, Roebroeck A, Daunizeau J *et al.* Effective connectivity: influence, causality and biophysical modeling. *Neuroimage* 2011; **58**: 339–61.
33. Friston KJ, Bastos AM, Oswal A *et al.* Granger causality revisited. *Neuroimage* 2014; **101**: 796–808.

34. Garcia Reyes R, Wang Y, Li M *et al.* Multivariate intrinsic local polynomial regression on isometric riemannian manifolds: applications to symmetric positive data. *Front Appl Math Stat* 2025; **11**: 1690557.
35. Dhamala M, Rangarajan G and Ding M. Analyzing information flow in brain networks with nonparametric granger causality. *Neuroimage* 2008; **41**: 354–62.
36. Li M, Wang Y, Lopez-Naranjo C *et al.* Harmonized-multinational qeeg norms (harmnqeeg). *Neuroimage* 2022; **256**: 119190.
37. Lemarechal JD, Jedynak M, Trebaul L *et al.* A brain atlas of axonal and synaptic delays based on modelling of cortico-cortical evoked potentials. *Brain* 2022; **145**: 1653–67.
38. Fort G, Risser L, Atchade Y *et al.* Stochastic fista algorithms: so fast? *2018 IEEE Statistical Signal Processing Workshop* (2018) 796–800.
39. Hedrich T, Pellegrino G, Kobayashi E *et al.* Comparison of the spatial resolution of source imaging techniques in high-density eeg and meg. *Neuroimage* 2017; **157**: 531–44.
40. Yeo BTT, Krienen FM, Sepulcre J *et al.* The organization of the human cerebral cortex estimated by intrinsic functional connectivity. *J Neurophysiol* 2011; .
41. Wang Q, Valdes-Hernandez PA, Paz-Linares D *et al.* Eecog-comp: an open source platform for concurrent eeg/ecog comparisons—applications to connectivity studies. *Brain Topogr* 2019; **32**: 550–68.
42. Ding L, Duan W, Wang Y *et al.* Test–retest reproducibility comparison in resting and mental task states: a sensor- and source-level eeg spectral analysis. *Int J Psychophysiol* 2022; **173**: 20–28.
43. Li N, Yang J, Long C *et al.* Test–retest reliability of eeg aperiodic components in resting and mental task states. *Brain Topogr* 2024; **37**: 961–71.
44. Shrout PE and Fleiss JL. Intraclass correlations: uses in assessing rater reliability. *Psychol Bull* 1979; **86**: 420.
45. Yao D. *The physics and mathematics of electroencephalogram*, (CRC Press2024).
46. Burt JB, Demirtas M, Eckner WJ *et al.* Hierarchy of transcriptomic specialization across human cortex captured by structural neuroimaging topography. *Nat Neurosci* 2018; **21**: 1251–9.
47. Bastos AM, Vezoli J, Bosman CA *et al.* Visual areas exert feedforward and feedback influences through distinct frequency channels. *Neuron* 2015; **85**: 390–401.
48. Michalareas G, Vezoli J, Van Pelt S *et al.* Alpha-beta and gamma rhythms subserve feedback and feedforward influences among human visual cortical areas. *Neuron* 2016; **89**: 384–97.
49. Park J, Ho RLM, Wang WE *et al.* The effect of age on alpha rhythms in the human brain derived from source localized resting-state electroencephalography. *Neuroimage* 2024; **292**: 120614.
50. Bosch-Bayard J, Valdes-Sosa P, Virues-Alba T *et al.* 3d statistical parametric mapping of eeg source spectra by means of variable resolution electromagnetic tomography (vareta). *Clin Electroencephalogr* 2001; **32**: 47–61.
51. Turner C, Baylan S, Bracco M *et al.* Developmental changes in individual alpha frequency: recording eeg data during public engagement events. *Imaging Neurosci* 2023; **1**: 1–14.
52. Zhang X, Guo B and Yi N. Zero-inflated gaussian mixed models for analyzing longitudinal microbiome data. *PLoS One* 2020; **15**: e0242073.
53. Grydeland H, Vertes PE, Vasa F *et al.* Waves of maturation and senescence in micro-structural mri markers of human cortical myelination over the lifespan. *Cereb Cortex* 2019; **29**: 1369–81.
54. de Faria Jr O, Pivonkova H, Varga B *et al.* Periods of synchronized myelin changes shape brain function and plasticity. *Nat Neurosci* 2021; **24**: 1508–21.
55. Rushton WAH. A theory of the effects of fibre size in medullated nerve. *J Physiol* 1951; **115**: 101.
56. Valdes-Hernandez PA, Ojeda-Gonzalez A, Martinez-Montes E *et al.* White matter architecture rather than cortical surface area correlates with the eeg alpha rhythm. *Neuroimage* 2010; **49**: 2328–39.
57. Becker R, Knock S, Ritter P *et al.* Relating alpha power and phase to population firing and hemodynamic activity using a thalamo-cortical neural mass model. *PLoS Comput Biol* 2015; **11**: e1004352.
58. Rosen BQ and Halgren E. An estimation of the absolute number of axons indicates that human cortical areas are sparsely connected. *PLoS Biol* 2022; **20**: e3001575.
59. Valdes-Sosa PA, Sanchez-Bornot JM, Lage-Castellanos A *et al.* Estimating brain functional connectivity with sparse multivariate autoregression. *Phil Trans R Soc B* 2005; **360**: 969–81.
60. Areces-Gonzalez A, Paz-Linares D, Riaz U *et al.* Ciftistorm pipeline: facilitating reproducible eeg/meg source connectomics. *Front Neurosci* 2024; **18**: 1237245.
61. Ding L, Worrell GA, Lagerlund TD *et al.* Ictal source analysis: localization and imaging of causal interactions in humans. *Neuroimage* 2007; **34**: 575–86.